

# Wind Power at Sea as Observed from Space

W. Timothy Liu, Wenqing Tang, and Xiaosu Xie  
*Jet Propulsion Laboratory, California Institute of Technology,  
 USA*

## 1. Introduction

With the increasing demand of electric power and the need of reducing greenhouse gas emission, the importance of turning wind energy at sea into electric power has never been more evident. For example, China is vigorously studying and pursuing the potential of wind energy to lessen dependence of coal consumption (McElroy et al., 2009). The White Paper on Energy (DTI, 2007) lays out an ambitious plan to the British Parliament in meeting the Renewables Obligation with offshore wind energy. The paper posted a challenge not only to Denmark, the leader of European offshore wind energy, but also to the world. New technology has also enabled floating wind-farms in the open seas to capture the higher wind energy and reduce the environmental impact on the coastal regions. Detailed distribution of wind power density ( $E$ ), as defined in Section 4, at sea is needed to optimize the deployment of such wind farms. The distribution is discussed in Section 5.

Just a few decades ago, almost all ocean wind measurements came from merchant ships. However, the quality and geographical distribution of these wind reports were uneven. Today, operational numerical weather prediction (NWP) also gives us wind information (Capps & Zender, 2008), but NWP depends on numerical models, which are limited by our knowledge of the physical processes and the availability of data. Recently, spacebased microwave sensors are giving us wind information with sufficient temporal and spatial sampling, night and day, under clear and cloudy conditions. Results from the most advanced passive sensor, which measures only wind speed, and active sensor, which measures both speed and direction, will be discussed. The principles of wind retrievals by active and passive microwave sensors are described in Section 2 and 3 respectively. The dependence of wind speed on height above sea level and on atmospheric stability is discussed in Section 6 and 7.

## 2. Scatterometer

The capability of the spacebased scatterometer in measuring wind vector at high spatial resolution is discussed by Liu (2002) and Liu and Xie (2006). The scatterometer sends microwave pulses to the Earth's surface and measures the backscatter power. Over the ocean, the backscatter power is largely caused by small centimeter-scale waves on the surface, which are believed to be in equilibrium with stress ( $\tau$ ). Stress is the turbulent momentum transfer generated by vertical wind shear and buoyancy. Liu and Large (1981) demonstrated, for the first time, the relation between measurements by a spacebased scatterometer and surface stress measured on research ships. Although the scatterometer

has been known to measure  $\tau$ , it has also been promoted as a wind-measuring instrument. The geophysical data product of the scatterometer is the equivalent neutral wind,  $U_N$ , at 10 m height (Liu and Tang 1996), which, by definition, is uniquely related to  $\tau$ , while the relation between  $\tau$  and the actual winds at the reference level depends on atmosphere stability and ocean's surface current.  $U_N$  has been used as the actual wind, particularly in operational weather applications. The difference between the variability of stress and wind is assumed to be negligible because the marine atmosphere has near neutral stratification, and that the magnitude of ocean current is small relative to wind speed over most ocean areas. Because stress is small-scale turbulence generated by buoyancy and wind shear, its magnitude should have strong spatial coherence with sea surface temperature and its direction should show influence by current. These features that are driven by ocean processes may not be fully represented in winds that are subjected to larger-scale atmospheric factors, as discussed by Liu and Xie (2008) and Liu et al. (2010).

NASA launched a Ku-band scatterometer, QuikSCAT, in June 1999. Level-2 data at 12.5 km resolution are obtained from the Physical Oceanography Distributed Active Archive Center. Seven years of the data, from June 2002 to May 2009 (coincide with radiometer data as discussed in Section 3), organized in wind vector cells along satellite swath, are binned into uniform  $1/8$  degree grids over global oceans and fitted to the Weibull distribution for the 7 year periods. There is hardly any in situ stress measurement. Even for winds, there is no in situ measurement that could represent the range of scatterometer data, particularly at the high and low ends, to evaluate the probability density function (PDF) from which  $E$  is derived.

### 3. Microwave radiometer

Ocean surface wind speed can also be derived from the radiance observed by a microwave radiometer. It is generally believed that wind speed affects the surface emissivity indirectly through the generation of ocean waves and foam (Hollinger, 1971; Wilheit, 1979). Radiometers designed to observe the ocean surface operate primarily at window frequencies, where atmospheric absorption is low. To correct for the slight interference by tropospheric water vapor, clouds, and rainfall and, to some extent, the effect of sea surface temperature, radiances at frequencies sensitive to sea surface temperature, atmospheric water vapor, and liquid water are also measured (Wentz, 1983). The Advanced Microwave Scanning Radiometer-Earth Observing System (AMSR-E), on board of NASA's Aqua satellite, was launched in May 2002 and has been measuring ocean parameters including wind speed and sea surface temperature. These parameters averaged to  $0.25^\circ$  grids for ascending and descending paths were obtained from Remote Sensing System.

### 4. Power density

The Weibull distribution (Gaussian and Rayleigh distributions are special cases of it) has been often used to characterize the PDF of wind power (e.g., Pavia & O'Brien 1986). A two parameters Weibull distribution has the PDF ( $p$ ) as a function of wind speed  $U$ ,

$$p(U) = (k/c)(U/c)^{k-1} \exp[-(U/c)^k] \quad (1)$$

where  $k$  is the dimensionless shape parameter, and  $c$  is the scale parameter. A number of methods to estimate Weibull parameters exist, with negligible difference in the results (Monahan, 2006). We used the simplest formula:

$$c = \bar{U}/\Gamma(1+1/k) \quad (2a)$$

$$k = (\bar{U}/\sigma)^{1.086} \quad (2b)$$

where  $\bar{U}$  is the mean,  $\sigma$  is the standard deviation of wind speed, and  $\Gamma$  is the gamma function. The available wind power density  $E$  (which is proportional to  $U^3$ ) may be calculated from the Weibull distribution parameters as

$$E = \frac{1}{2} \rho c^3 \Gamma(1+3/k) \quad (3)$$

where  $\rho$  is the air density.  $E$  is essentially the kinetic energy of the wind.

We will analyze PDF and  $E$ , which will provide the characteristics of not only the means and the frequencies of strong wind, but also the variation and higher moments critical in relating the non-linear effects of wind on electric power generation capability.

## 5. Geographic distribution

Scatterometer climatology in forms of mean wind (e.g., Risien & Chelton, 2006), frequency of strong wind (Sampe & Xie, 2007), and power density (Liu et al., 2008a) have been produced before. The PDF of 7 year of wind speed at 10 m height above oceans between 75° latitudes (Fig. 1) shows the slight difference between QuikSCAT and AMSR-E. AMSR-E, which peaks at 7.5 m/s, has more high wind than QuikSCAT, which peaks at 7 m/s. The global distributions of  $E$  (Fig. 2 and 3) are very similar, with AMSR-E data giving a slightly larger dynamic range.

The distributions of  $E$ , as shown in Fig. 2 and 3, confirm the conventional knowledge: strongest  $E$  is found over the mid-latitude storm tracks of the winter hemisphere, the relatively steady trade winds over the tropical oceans, and the seasonal monsoons. At mid-

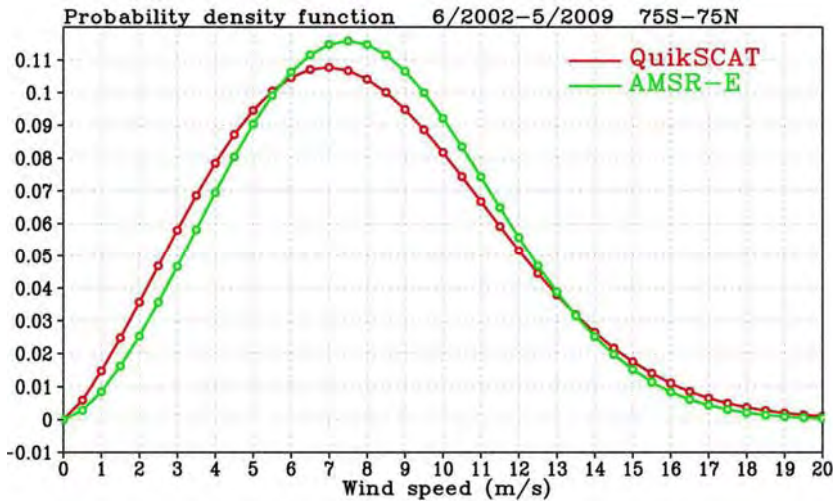


Fig. 1. Comparison of the probability density function of ocean surface wind speed from 7 years of QuikSCAT and AMSR-E measurements.

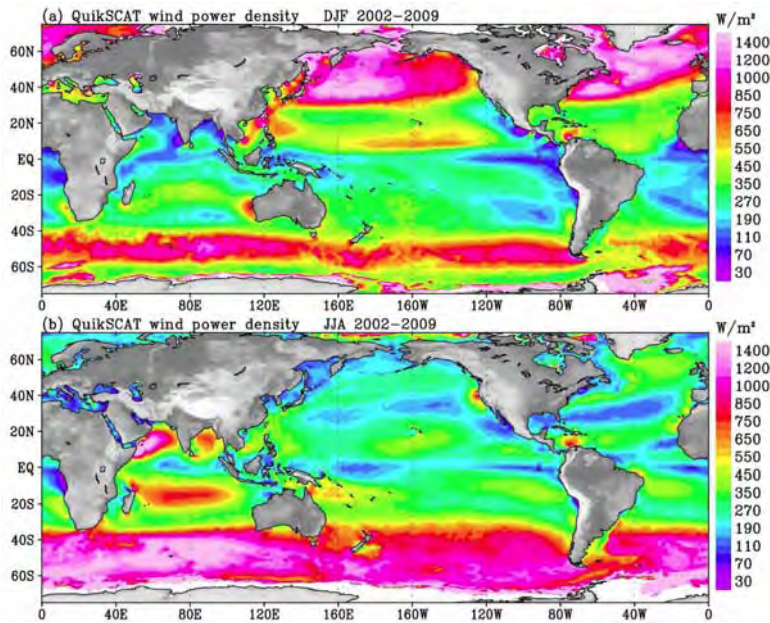


Fig. 2. Distribution of power density of ocean surface wind (10 m) from QuikSCAT for (a) boreal winter (December, January, and February) and (b) boreal summer (June, July, and August).

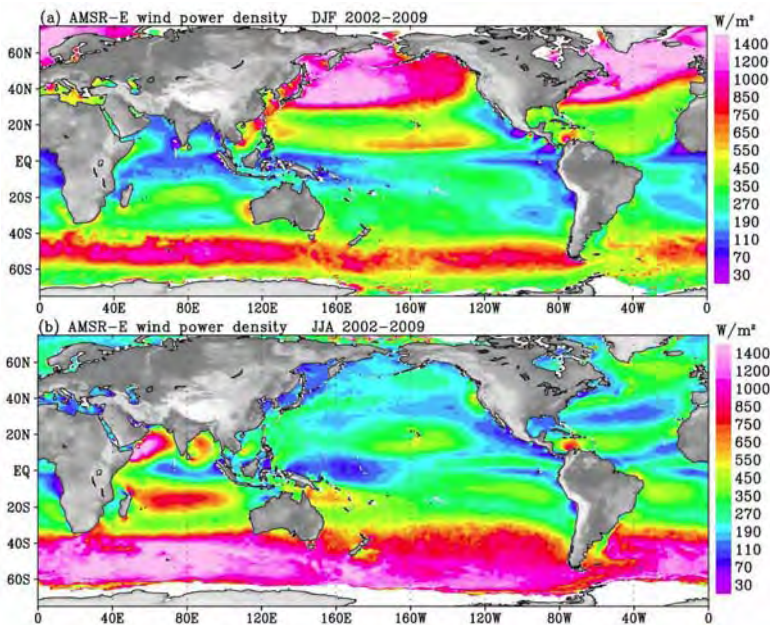


Fig. 3 Same as Fig. 2, but from AMSR-E.

latitude in the winter hemisphere,  $E$  is much larger than those in the tropics, making the display of the major features with the same color scale extremely difficult. The trade winds, particularly in the western Pacific and Southern Indian oceans are stronger in winter than summer, but the seasonal contrast is much less than those of the mid-latitude storm track. In the East China Sea, particularly through the Taiwan and Luzon Strait, the strong  $E$  is caused by the winter monsoon. In the Arabian Sea and Bay of Bengal, it is caused by the summer monsoon. In the South China Sea, the wind has two peaks, both in summer and winter. QuikSCAT data also reveal detailed wind structures not sufficiently identified before. The strong winds of transient tropical cyclones are not evident in  $E$  derived from the seven-year ensemble.

Because space sensors measure stress, the distribution reflects both atmospheric and oceanic characteristics. Regions of high  $E$  associated with the acceleration of strong prevailing winds when deflected by protruding landmasses are ubiquitous. Less well-known examples, such as the strong  $E$  found downwind of Cape Blanco and Cape Mendocino in the United States and Peninsula de La Guajira in Columbia, stand out even on the global map. Strongest  $E$  is observed when the along-shore flow coming down from the Labrador Sea along the west Greenland coast as it passes over Cape Farewell meeting wind flowing south along the Atlantic coast of Greenland. Strong  $E$  is also found when strong wind blows offshore, channeled by topography. The well-known wind jets through the mountain gap of Tehuantepec in Mexico and the Mistral between Spain and France could be discerned in the figures. Alternate areas of high and low  $E$  caused by the turbulent production of stress by buoyancy could also be found over mid-latitude ocean fronts, with strong sea surface temperature gradient (e.g., Liu & Xie, 2008), particularly obvious over the semi-stationary cold eddy southeast of the Newfoundland.

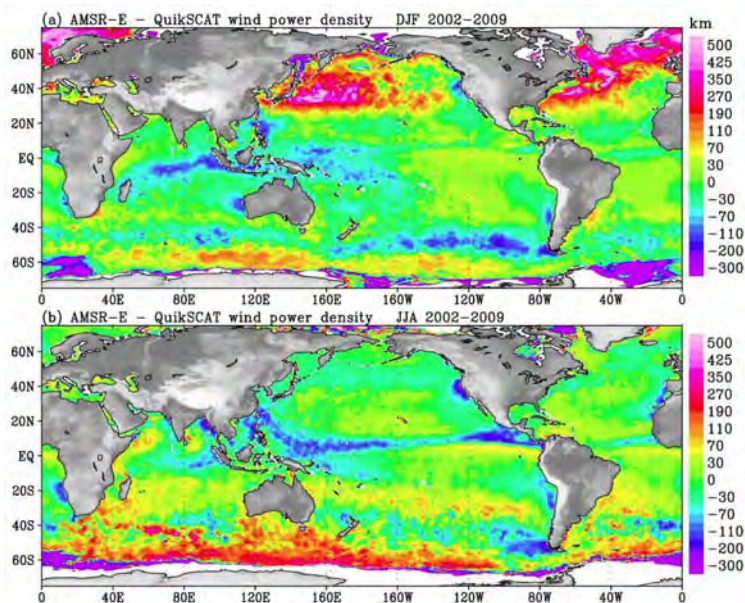


Fig. 4. Difference of wind power density between AMSR-E and QuikSCAT for (a) boreal winter and (b) boreal summer.



Fig. 4 shows that  $E$  from AMSR-E is higher than that from QuikSCAT in the winter hemisphere at mid to high latitudes of both Pacific and Atlantic, and slightly lower in the tropics. The large differences around Antarctica may be due to contamination of scatterometer winds by ice.

## 6. Height dependence

The analysis, so far, is based on the equivalent neutral wind at 10 m, the standard height of scientific studies. The effective heights of various designs of the wind turbines, from the lower floating turbine that spins around a vertical axis to the anchored ones that spin around a horizontal axis, are likely to be different. The turbine height dependence has been well recognized (e.g. Barheltm, 2001). There is a long history of studying the wind profile in the atmospheric surface (constant flux) layer in term of turbulent transfer. The flux-profile relation (also called similarity functions) of wind, as described by Liu et al. (1979), is

$$\frac{U - U_s}{U_*} = 2.5 \left( \ln \frac{Z}{Z_0} - \psi \right) = \frac{1}{\sqrt{C_D}} \quad (4)$$

where  $U_s$  is the surface current,  $U_* = (\tau/\rho)^{1/2}$  is the frictional velocity,  $\rho$  is the air density,  $Z_0$  is the roughness length,  $\Psi$  is the function of the stability parameter, and  $C_D$  is the drag coefficient. The stability parameter is the ratio of buoyancy to shear production of turbulence. The effect of sea state and surface waves (e.g., Donelan et al. 1997) are not included explicitly in the relation.  $U_*$  and  $Z_0$  are estimated from the slope and zero intercept respectively of the logarithmic wind profile. The drag coefficient is an empirical coefficient in relating  $\tau$  to  $\rho U^2$  (Kondo 1975, Smith 1980, Large & Pond, 1981) and is expressed as a function of wind speed. An alternative to using the drag coefficient is to express  $Z_0$  as a function of  $U_*$ . For example, Liu and Tang (1996) incorporated such a relation in solving the similarity function. They combined a smooth flow relation with Charnock's relation in rough flow to give

$$Z_0 = 0.11 \frac{\nu}{U_*} + 0.011 \frac{U_*^2}{g} \quad (5)$$

where  $\nu$  is the kinematic viscosity and  $g$  is the acceleration due to gravity.

In general oceanographic applications, the surface current is assumed to be small compared with wind and the atmosphere is assumed to be nearly neutral. With the neglect of  $U_s$  and  $\Psi$  in (1),  $U$  becomes  $U_N$  by definition. The wind speed at a certain height  $z$  ( $U_z$ ) relative to  $U_N$  at 10 m,  $U_{10}$ , is given by

$$\frac{U_z}{U_{10}} = 1 + 2.5 \sqrt{C_D} \ln \left( \frac{z}{10} \right) \quad (6)$$

and  $z$  is in meter. Fig 5 shows the variation of wind speed at 80 m as a function of wind speed at 10 m, under neutral conditions for three formulations of the drag coefficient. For example, the 80 m wind exceeds 10 m wind by 5% and 20% at wind speed of 10 m/s and 30 m/s respectively, according to the drag coefficient given by Kondo (1975).

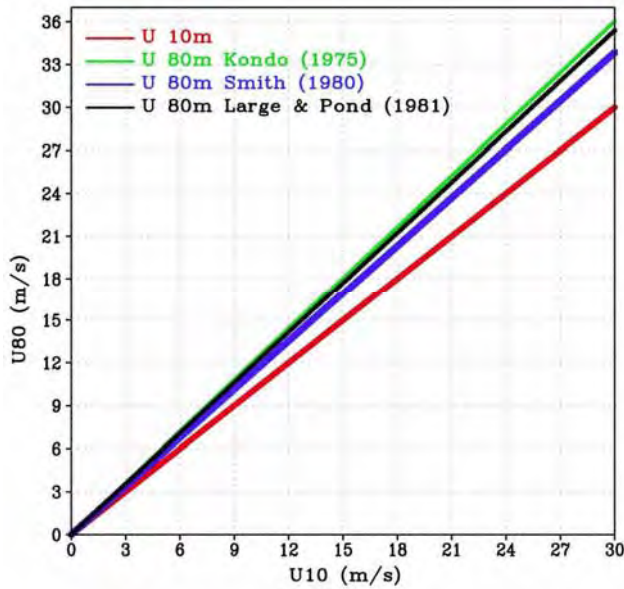


Fig. 5. Wind speed at 80 m height as a function of wind speed at 10 m under neutral stability for three formulations of drag coefficient.

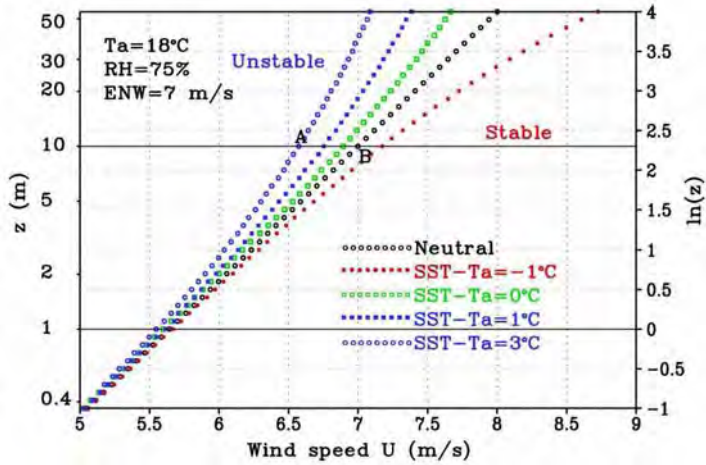


Fig. 6. Comparison of wind profiles under various stability conditions.

## 7. Stability dependence

Typical wind profiles at various stabilities are shown in Fig. 6. At a given level,  $U_N$  is larger than the actual wind under unstable condition but lower under stable condition. From (4) the difference Between  $U_N$  and the actual wind  $U$  is

$$\delta U = U_N - U = 2.5U * \psi \quad (7)$$

As described by Liu et al. (1979) and the computer program in Liu and Tang (1996), the flux profile relations for wind, temperature, and humidity could be solved simultaneously for inputs of wind speed, temperature, and humidity at a certain level and the sea surface temperature to yield the fluxes of momentum (stress), heat, and water vapor. The value of  $\Psi$  is a by-product. Using  $U_N$  provided by QuikSCAT, sea surface temperature from AMSR-E, air temperature, and humidity from the reanalysis of the European Center for Medium-range Weather Forecast,  $\delta U$  at 10 m averaged over a three years period, for January and July, are computed and shown in Fig. 7. The distribution of stability effect on wind speed closely follows the distribution of sea-air temperature difference shown in Fig. 8.

$U_N$  is higher than  $U$  in the unstable regions and lower in stable regions.  $U_N$  is higher than  $U$  by as much as 0.7 m/s in January over the western boundary currents. It is also higher than  $U$  over the intertropical convergence zone, the south Pacific convergence zone, and the South Atlantic convergence zone.  $U_N$  is lower than  $U$  in stable regions, such as over the circumpolar current and in northeast parts of both Pacific and Atlantic.

## 8. Future potential and conclusion

One polar orbiter could sample the earth, at most, two times a day and may introduce error in  $E$  because of sampling bias, as discussed by Liu et al. (2008b) in constructing the diurnal cycle with data from tandem missions. There are three scatterometers in operation now. QuikSCAT or the similar scatterometer on Oceansat-2 launched recently by India, will covered 90% of the ocean daily, and the Advanced Scatterometer (ASCAT) on the European Meteorology Operational Satellite (METOP) will covered similar area in two days, as showed in Fig. 9.

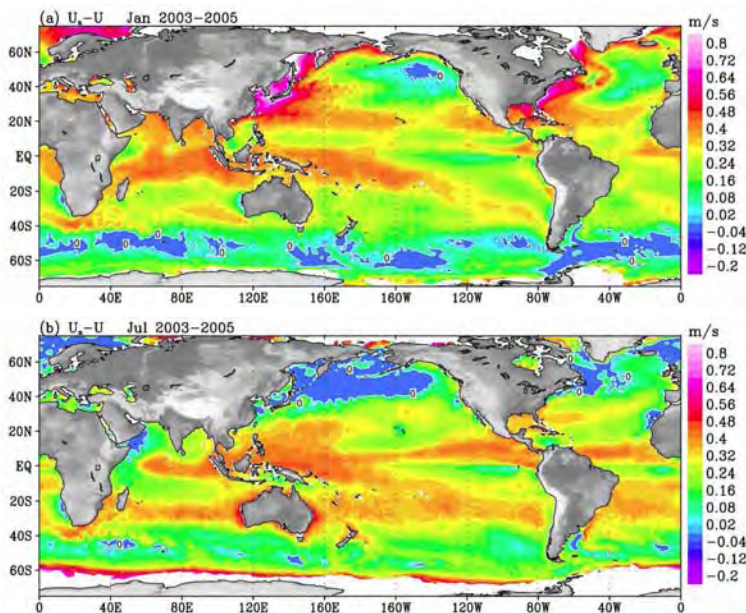


Fig. 7. Difference between equivalent neutral wind and actual wind at 10 m for (a) January and (b) July.



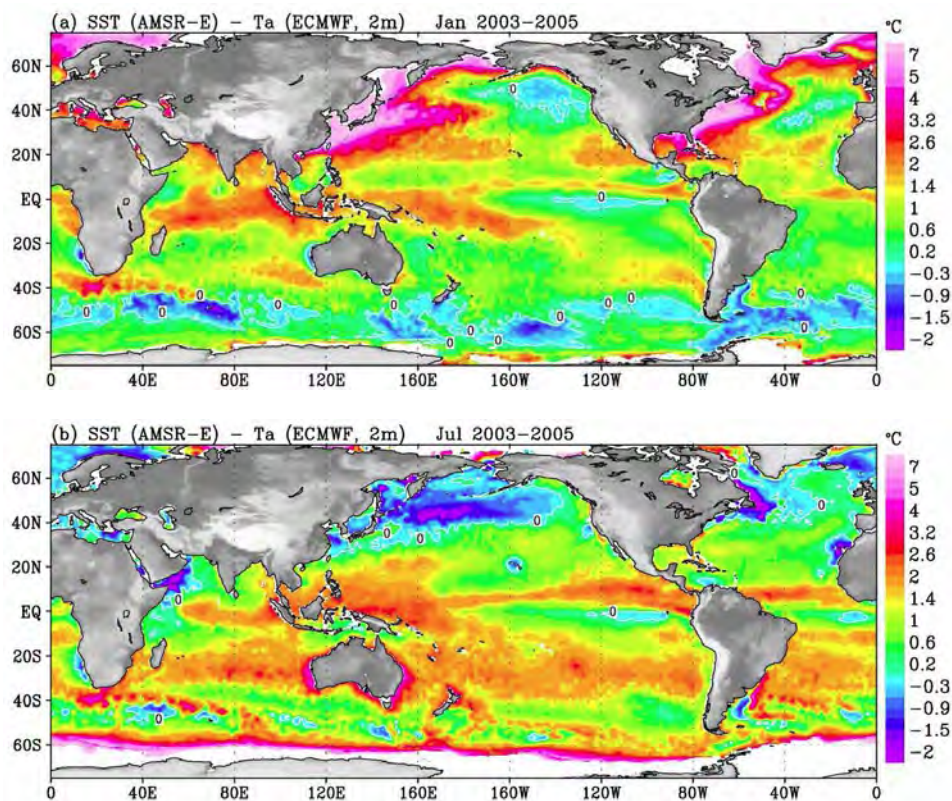


Fig. 8. Difference between sea surface temperature and air temperature (2 m) for (a) January and (b) July.

QuikSCAT alone could resolve the inertial period required by the oceanographers only in the tropical Oceans, but the combination of QuikSCAT and ASCAT will cover the inertial period at all latitudes, as shown in Fig. 10. Even the combination of QuikSCAT and ASCAT would not provide six hourly revisit period, as required by operational meteorological applications, over most of the oceans. The addition of Oceansat-2 brings the revisit interval close to 6-hour at all latitudes. The scatterometer on Chinese Haiyang-2 satellites, approved for 2011 launch, will shorten the revisit time or will make up the sampling loss at the anticipated demise of the aging QuikSCAT. As shown in Fig. 9 and 10, the combination of these missions will meet the 6 hourly operational NWP requirement in addition to the inertial frequency required by the oceanographers.

Deriving a consistent merged product may need international cooperation in calibration, and maintaining them over time may require political will and international support. It remains a technical challenge to generate electricity by wind off shore and transmit the power back for consumption efficiently, but satellite observations could contribute to realize the potential.

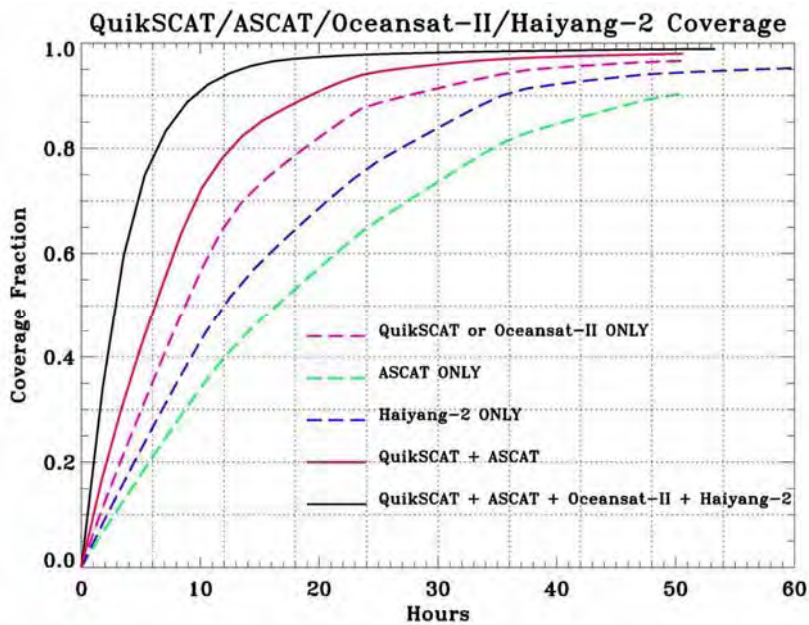


Fig. 9 Fractional coverage, between 70°N and 70°S by various tandem missions as a function of time.

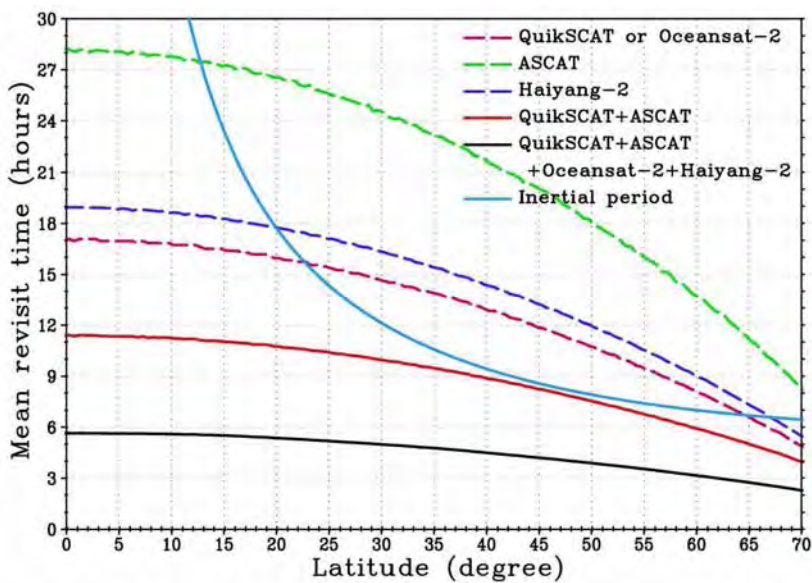


Fig. 10 The latitudinal variation of zonally averaged revisit interval for various tandem missions.

## 9. Acknowledgment

This study was performed at the Jet Propulsion Laboratory, California Institute of Technology under contract with the National Aeronautics and Space Administration (NASA). It was jointly supported by the Ocean Vector Winds and the Physical Oceanography Programs of NASA. © 2009 California Institute of Technology. Government sponsorship acknowledged.

## 10. References

- DTI, 2007: Meeting the Energy Challenge: A White Paper on Energy, Department of Trade and Industry, 341 pp. The Stationary Office, London, United Kingdom.
- Barthelmie, R. J., 2001: Evaluating the impact of wind induced roughness change and tidal range on extrapolation of offshore vertical wind speed profiles. *Wind Energy*, 2001; 4:99-105 (DOI: 10.1002/we.45).
- Capps, S.B., and C.S. Zender, 2008: Observed and CAM3 GCM sea surface wind speed distributions: Characterization, comparison, and bias reduction. *J. Clim.*, 21, 6569-6585.
- Donelan, M.A., W.M. Drenan, and K.B. Katsaros, 1997: The air-sea momentum flux in conditions of wind sea and swell. *J. Phys. Oceanogr.*, 27, 2087-2099.
- Hollinger, J. P. 1971. Passive microwave measurements of sea surface roughness. *IEEE Trans. Geosci. Electronics* GE-9:165-169.
- Kondo, J., 1975: Airsea bulk transfer coefficients in diabatic conditions. *Bound-Layer Meteor.*, 9, 91-112.
- Large, W.G., and S. Pond, 1981: Open ocean momentum flux measurements in moderate to strong winds. *J. Phys. Oceanogr.*, 11, 324-336.
- Liu, W.T., 2002: Progress in scatterometer application, *J. Oceanogr.*, 58, 121-136.
- Liu, W.T., and W.G. Large, 1981: Determination of surface stress by Seasat-SASS: A case study with JASIN Data. *J. Phys. Oceanogr.*, 11, 1603-1611.
- Liu, W.T., and W. Tang, 1996: Equivalent Neutral Wind. JPL Publication 96-17, Jet Propulsion Laboratory, Pasadena, 16 pp.
- Liu, W.T., and X. Xie 2006: Measuring ocean surface wind from space. *Remote Sensing of the Marine Environment, Manual of Remote Sensing*, Third Edition, Vol. 6, J. Gower (ed.), Amer. Soc. for Photogrammetry and Remote Sens. Chapter 5, 149-178.
- Liu, W.T., and X. Xie, 2008: Ocean-atmosphere momentum coupling in the Kuroshio Extension observed from Space. *J. Oceanogr.*, 64, 631-637.
- Liu, W.T., K.B. Katsaros, and J.A. Businger, 1979: Bulk parameterization of air-sea exchanges in heat and water vapor including the molecular constraints at the interface. *J. Atmos. Sci.*, 36, 1722-1735.
- Liu, W.T., W. Tang, and X. Xie, 2008a: Wind power distribution over the ocean. *Geophys. Res. Lett.*, 35, L13808, doi:10.1029/2008GL034172.
- Liu, W.T., W. Tang, X. Xie, R. Navalgund, and K.Xu, 2008b: Power density of ocean surface wind-stress from international scatterometer tandem missions. *Int. J. Remote Sens.*, 29(21), 6109-6116.
- McElroy, M.B., X. Lu, C.P. Nielsen, and Y. Wang, 2009: Potential for wind-generated electricity in China. *Science*, 325, 1378-1380.

- Monahan, 2006: The probability distribution of sea surface wind speeds. Part I: theory and SeaWinds observations. *J. Clim.*, 19, 497-520.
- Pavia, E. G., and J. J. O'Brien, 1986: Weibull statistics of wind speed over the ocean, *J. Clim. Appl. Meteorol.*, 25, 1324-1332.
- Risien, C. M., and D. B. Chelton, 2006: A satellite-derived climatology of global ocean winds. *Remote Sens. Environ.*, 105, 221-236.
- Sampe, T., and S-P. Xie, 2007: Mapping high sea winds from space: a global climatology. *Bull. Amer. Meteor. Soc.*, 88, 1965-1978
- Smith, S.D., 1980: Wind stress and heat flux over the ocean in gale force winds. *J. Phys. Oceanogr.*, 10, 709-726.
- Wentz, F. J. 1983: A model function for ocean microwave brightness temperatures. *J. Geophys. Res.*, 88, 1892-1908.
- Wilheit, T. T. 1979: A model for the microwave emissivity of the ocean.s surface as a function of wind speed. *IEEE Trans. Geoscience Electronics* GE-17, 244-249.